Hybrid Photon-Plasmon Coupling and Ultrafast Control of Nanoantennas on a Silicon Photonic Chip

Bigeng Chen,[†] *Roman Bruck,*[†,§] *Daniel Traviss,* [†,§] *Ali Z. Khokhar,*[‡] *Scott Reynolds,* [‡] *David J. Thomson,* [‡] *Goran Z. Mashanovich,* [‡] *Graham T. Reed,* [‡] *and Otto L. Muskens.*[*, †]

[†] Physics and Astronomy, Faculty of Physical Sciences and Engineering, University of Southampton, Southampton SO17 1BJ, UK

[‡] Optoelectronics Research Centre, Faculty of Physical Sciences and Engineering, University of Southampton, Southampton SO17 1BJ, UK.

KEYWORDS Nanoantennas, Plasmonics, Silicon Photonics, Coherent Perfect Absorption (CPA)

ABSTRACT Hybrid integration of nanoplasmonic devices with silicon photonic circuits holds promise for a range of applications in on-chip sensing, field-enhanced and nonlinear spectroscopy, and integrated nanophotonic switches. Here, we demonstrate a new regime of photon-plasmon coupling by combining a silicon photonic resonator with plasmonic nanoantennas. Using principles from coherent perfect absorption, we make use of standing-wave light fields to maximize the photon-plasmon interaction strength. Precise placement of the broadband antennas with respect to the narrowband photonic racetrack modes results in controlled hybridization of

only a subset of these modes. By combining antennas into groups of radiating dipoles with opposite phase, far-field scattering is effectively suppressed. We achieve ultrafast tuning of photon-plasmon hybridization including reconfigurable routing of the standing-wave input between two output ports. Hybrid photonic-plasmonic resonators provide conceptually new approaches for on-chip integrated nanophotonic devices.

Coherent perfect absorption (CPA) is realized by having two counter-propagating waves interfere constructively or destructively in an absorptive system.[1, 2] Within a cavity, CPA acts as time reversed lasing, where only specific resonances are subject to absorption.[3, 4] These novel properties have intrigued vast interest with potential applications such as interferometric optical devices[5, 6] and lasing mode manipulation.[7] High contrast optical modulation using CPA has been demonstrated in studies by free-space illumination,[3, 5] but few were shown experimentally on photonic integrated circuits,[8] which are essential for on-chip optical communication and signal processing systems. Non-resonant, nanoscale coherent absorbers were used as mode selectors in PT-symmetric systems on an InGaAsP ring resonator with gain.[7] In a numerical study, a configuration employing resonant nanoantennas as coherent perfect absorbers on silicon waveguides was proposed resulting in large extinction ratio and small insertion loss.[9]

The combination of CPA with plasmonic nanoantennas is of interest as a strategy for maximizing the conversion efficiency of incident light to the optical near-field. Nanoantennas offer strong interaction with optical fields[10-12] and nanoscale confinement of energy.[13, 14] Integration of nanoplasmonic devices with photonic integrated circuits enables new ultra-compact devices with footprints comparable to nanoelectronics.[15] Recent applications of plasmonic nanoantennas in photonic integrated circuits have included directional coupling,[16-18] routing,[19] plasmon-enhanced sensing,[20, 21] and nano-focusing.[22] Moreover, the combination of plasmonic nanoantennas and photonic resonators can access new regimes of hybrid light-matter interaction with a tuneable Purcell factor.[23]

Here, we demonstrate experimentally the coherent interactions between nanoantennas and a silicon photonic racetrack resonator in a CPA geometry. Similar to antennas placed inside a conventional microcavity,[24] the precise positioning of nanoantennas onto the racetrack allows selective coupling to specific photonic modes when using a standing-wave incident light field. We use both optical transmission and darkfield imaging of scattered light from the antennas to quantify the coupling strength in the hybrid photonic-plasmonic system. Active control over the coupling efficiency is obtained using ultrafast pulsed laser excitation of the waveguide, resulting in a shift of the standing-wave pattern and hence a modulation of the antenna excitation. The design combining coherent absorption in plasmonic antennas on waveguides holds promise as a new approach to ultrafast control of plasmonic near-fields and nanophotonic switching in silicon photonics.

Devices were fabricated from a silicon-on-insulator (SOI) wafer (220-nm-thick top silicon layer, 2-μm-thick buried oxide) using electron beam lithography and reactive ion etching. Rib waveguides of 450 nm width and 120 nm etch depth were used to form the circuits. Only the fundamental TE mode is supported in these single-mode waveguides. Grating couplers were used to couple light in and out of the chip. Following the fabrication of the silicon photonic circuit, we performed a second electron beam lithography and subsequent gold deposition to fabricate the nanoantennas on top of the silicon waveguides. The antennas were designed with length of 150 nm, width of 80 nm, and height of 25 nm, to reach a surface plasmon resonance at the design wavelength of around 1550 nm, with a resonance bandwidth covering the entire C-band.

The main part of the photonic circuit is shown in Figure 1a. Two mutually coherent outputs of a 1x2 multimode interference (MMI) device are coupled into a racetrack resonator from opposite directions. The racetrack, with a perimeter of 78.8 μm, is shown in the scanning electron microscopy (SEM) image of Figure 1b. In the racetrack, the counter-propagating waves produce a standing-wave electromagnetic field pattern. Light travelling through the resonator is coupled out into a drop waveguide, carrying light in both directions away from the resonator towards two grating couplers for outcoupling. We specifically chose this structure as it allows investigating the CPA in transmission devices as such devices are of greater interest in real-world applications. Designs for reflection-type devices were outlined in Ref. 9.

The arrangement under study consists of two sets of plasmonic antennas on the resonator, one quarter of its circumference in both directions from the point of incoupling [see Figure 1b]. Zoomed-in images of antennas on the racetrack are shown in Figures 1c-e for three different devices. In this configuration, the interaction between the antennas and a photonic resonance is defined by the exact spatial positioning of the antennas in the standing wave intensity pattern. In the limit of weak interaction, perturbation of the purely photonic modes by the antennas is negligible and the total field E is given by the superposition of clockwise (E_c) and counter-clockwise (E_{cc}) modes, $E=E_c e^{i\Delta\varphi}+E_{cc}$, where $\Delta\varphi$ is the phase difference of the two input waves. The amount of coupling to the antennas in this case is determined by the intensity of the standing wave of the photonic mode at the position of the antennas, which follows as:

$$I(l) = |E(l)|^2 = \left|E_0 e^{i(\omega t + kl + \Delta\varphi)} + E_0 e^{i(\omega t - kl)}\right|^2$$

$$= 2E_0^2\left[1 + \cos\left(\frac{4N\pi l}{L} + \Delta\varphi\right)\right] \qquad (1)$$

where I is the intensity, l is the position along the racetrack, L is the perimeter of the racetrack, N is the resonance index. The spatial coordinate l is defined clockwise with respect to the middle of the right vertical section ($l = 0$). In our experimental arrangement where light from the MMI is coupled through equal path lengths, $\Delta\varphi = -180°$ and the intensity at the antenna positions $\pm L/4$ is $4E_0^2$ for odd modes and 0 for even modes. Thus, odd modes will exhibit maximum interaction with the antennas while even modes will travel the resonator unhindered. In general, $\Delta\varphi$ can be tuned by shifting the phase of one of the two input arms. To achieve CPA, the strength of the absorbers needs to be balanced for the application. Too weak absorbers will not induce sufficient absorption, while too strong absorption will decouple the two counter-propagating waves, thus destroying the standing wave pattern that is required for coherent absorption.[9] The intensity equation (1) is periodic in $\lambda/2 = (n_{\mathrm{eff}}L)/2N$. This allows placing groups of antennas, spaced by $\lambda/2$, instead of single antennas, around $\pm L/4$ to increase the interaction strength. The strength of the absorbers can also be finely tuned by changing the antenna size while keeping the resonant wavelength fixed. In our experimental studies we considered antennas of fixed size and between 1 and 5 antennas per group. All antenna groups were placed symmetrically around $\pm L/4$, thus the odd antenna groups are positioned to couple to odd photonic modes, while the even antenna groups are offset by $\pm\lambda/4$ and are designed to couple to the even photonic modes.

The static properties of resonators with and without antennas were investigated using a setup featuring a CW tuneable laser at telecom wavelength. Figure 1c shows transmission spectra of the racetrack with and without antennas. The spectra are normalized to half the intensity of a straight waveguide to account for the splitting of the input intensity at the MMI. The bare racetrack resonator without nanoantennas, shown by the black curve, shows a characteristic comb of transmission peaks in the drop ports with transmission efficiency of up to 75% and an envelope given by the MMI bandwidth. For the resonator with three antennas per group, we find a suppression of alternating peaks in the spectrum by 70% (4dB) [red curve in Figure 1c]. The unperturbed transmission peaks of the hybrid resonator have intensities, spectral resonance positions and linewidths closely matching those of the reference device. The perturbed peaks are asymmetric in shape with a maximum that is redshifted by around 1 nm with respect to the unperturbed device.

Next to the modified transmission of the hybrid racetrack-antenna system, we observed the out of plane scattering of the plasmonic antennas as a measure of the interaction strength. Scattered light was collected from the top of the device using a 100x, 0.5 numerical aperture (N.A.) near-infrared objective (Mitutoyo) and was imaged using an InGaAs infrared camera (Owl, Raptor Photonics). Figures 2a-f shows results obtained for the racetracks equipped with one and two nanoantennas [SEM images shown in Figures 2a and b], while results for devices with up to 5 antennas are shown in Figure S1 in Supporting Information. Spatial intensity maps are shown for the wavelengths of maximum scattering for the single antenna [odd mode at 1544.9 nm, Figure 2c] and two antennas [even mode at 1553.0 nm, Figure 2d]. By scanning the narrowband laser, spectrally resolved scattering intensities were extracted from the camera images, as shown in the corresponding spectra in Figures 2e and f. For the single antenna case, the intensity at the odd photonic mode is the highest, which is consistent with the stronger coupling of the antenna to this mode. The same trend is observed for all odd number of antennas (see Figure S1 in Supporting Information). The situation is reversed for the even antenna groups where the even modes show the strongest scattering intensity, in agreement with the design.

The devices under study show large differences in both the point spread function (PSF) and the absolute intensity of the scattering signals between odd and even numbers of antennas per group. The single nanoantenna device in Figure 2c shows a Gaussian shaped PSF for each antenna on the top and the bottom of the racetrack. However for the two nanoantennas in Figure 2d, the dark-field images show a different shape of the PSF consisting of two lobes. Similar PSFs were calculated numerically using 3D finite-difference time domain (FDTD) simulations as shown in Figures 2g and h. The calculated PSFs were obtained by back-propagation of the far-field scattered light over the experimental numerical aperture. The double-lobe pattern can be explained by the cancelling of the dipolar contribution to the scattered field by pairs of adjacent nanoantennas with opposite phases. The arrows in the lower panels of Figures 2a and b illustrate the phase of the standing wave E-field at the $\lambda/2$-spaced antennas. While adjacent antennas are driven with opposite phases through the high-index waveguide, for free-space radiation outside the waveguide, the antenna spacing is deeply sub-wavelength. Therefore the dipole radiation from the antennas cancels effectively over most of the angular range and only a higher order radiation mode remains. More generally, even numbers of nanoantennas show suppressed far-field scattering due to destructive interference, while for odd numbers of nanoantennas, the scattering intensity does not increase beyond that of a single antenna [see Figure S1 in Supporting Information]. The functionality of antennas as phased array on a waveguide was demonstrated in earlier studies using Fourier-plane imaging.[16]

The observed behaviour in wavelength-dependent transmission and scattering is consistent with coherent excitation of nanoantennas by the standing wave resonances of the racetracks. As a next step, we achieve modulation of the coherent excitation in a dynamic experiment, where we actively control the phase between the input arms. As depicted in Figure 3a, a phase shift $\Delta\varphi$ in one input arms leads to a spatial shift of the standing wave pattern, thus changing the coupling strength of the antennas to the photonic modes. In our experiments, we employ the ultrafast photomodulation technique,[25] which allows direct detection of ultrafast changes in the optical spectrum. The optical arrangement is illustrated in Figure 3b. An ultrafast pump laser of 417 nm centre wavelength and

140 fs pulse duration was focused onto one of the input waveguides via the 0.5 N.A. objective. A synchronized probe pulse was coupled into the device with a controlled time delay with respect to the pump, in order to characterize the transmission through the photonic circuit. The probe was a Fourier-limited pulse centred at around 1537 nm with a full-width-at-half-maximum of around 10 nm, generated using an optical parametric oscillator. The transmission spectrum of the probe was collected at one of the drop ports using a spectrometer equipped with an InGaAs CCD (Andor Shamrock & iDus). Ultrafast pumping of the silicon waveguides results in free-carrier generation, which produces changes of both the real and imaginary parts of the refractive index.[25] The setup allows precise scanning of the pump spot over the device, which gives spatial maps of the dependence of the device on the local perturbation.

Figure 3c shows spatial maps of the differential transmission, $\Delta T/T$, at 5 ps delay time, when scanning the pump over the input MMI loop [see scan area in Figure 3b] at a fluence of 15 pJ/μm^2. Two wavelengths are selected at 1536.4 nm and 1544.4 nm, corresponding to even and odd modes of the racetrack, respectively. Each map shows a flipping of the sign of the $\Delta T/T$ modulation when pumping the top and bottom arms. Comparing the two wavelengths, we also see that the sign of the maps is flipped between even and odd modes. Similar maps are obtained when detecting the bottom output [see Figure S2 in Supporting Information]. Figure 3d shows the ultrafast dynamics of the perturbation taken at the bottom of the MMI loop as indicated by the circles in Figure 3c. The exponential decay time is 148±2 ps, which is in the typical range of the carrier relaxation time for silicon.[26] The small signal of opposite sign at negative delay time is attributed to a thermo-optic phase shift resulting from stationary heating of the device by the 80-MHz repetition rate laser.[27] We emphasize that, by exciting only the input waveguides, we do not consider modulation of the gold antenna permittivity, or of the photonic resonator quality factor and resonance wavelengths, directly using our pump laser.

To investigate the observed trends in more detail we show in Figure 3e and f the spectra and $\Delta T/T$ collected from the top output, when pumping the input waveguide coupler at the bottom or top section, respectively. The unperturbed drop port spectra resemble the normalized spectra of Figure 1c multiplied by the spectral envelope of the probe laser. In a control experiment on the racetrack without antennas, we find that optical pumping of the bottom input coupler does not result in any change in the spectrum of the top output to within the experimental accuracy [see Figure S3a in Supporting Information]. In the absence of antennas, waves in both directions propagate independently and the top output is fed from the top input only. Thus, pumping of the bottom input coupler does not produce any cross-modulation effect for the top output in this case. In contrast, the racetrack with groups of three antennas exhibits a strong cross-modulation of the transmitted intensity as seen in Figure 3e. The cross-modulation effect in this case corresponds to an interaction of the two counter-propagating modes through the antenna absorption.[5] By shifting the spatial location of nodes and anti-nodes, the transmission intensity of even modes is decreased (red arrows), while that of odd modes is increased (green arrows). The corresponding differential response $\Delta T/T$ shows a relative increase for the odd modes by as large as 100%. It was confirmed that the behaviour is symmetric when measuring the lower output and modulating the top input arm [see Figure S3 and Figure S4 in Supporting Information].

The above cross-modulation scheme reveals an ultrafast shift of the nodes and anti-nodes, which provides an active control over the coupling of the incident light field to the nanoantennas. Intuitively, one might expect a similar modulation when exciting the opposite input loop due to the symmetry of the CPA modulation scheme. However, Figure 3f shows an opposite change in the transmission of the individual modes when directly modulating the path that contributes to the detected output. This surprising result shows that the interaction between antennas and racetrack cannot be simply explained by an intensity-dependent CPA effect, but involves a more complex hybridization of photonic and plasmonic modes as described below. Additionally we see a flat, wavelength independent reduction of the transmitted intensity, corresponding to $\Delta T/T$ of -25%, which is also seen for the reference device without antennas [Figure S3g in Supporting Information] and which corresponds to pump-induced losses in the modulated section.

In the above, the device with three antennas per group was used as a representative example taken from a full investigation involving devices with different numbers of antennas. Figure 4 summarizes the $\Delta T/T$ values in cross-modulation as a function of pump fluence up to 35 pJ/μm^2, extracted from the spectra shown in Figure S3g-l of the Supporting Information. Resonances corresponding to odd and even photonic modes are indicated by red and green shaded areas in each figure. The magnitude of the $\Delta T/T$ response increases for devices with up to three antennas per group, and no substantial increase is found for higher number of antennas, indicating that three antennas give the optimum interaction strength. Odd and even modes show a different sign of the $\Delta T/T$ response, which also depends on whether the number of antennas is odd or even, in line with their spatial arrangement around lines of symmetry $\pm L/4$ (dashed line in SEM images). This behaviour clearly visualizes how antenna placement dictates which resonances are absorbed. For pump fluences above 20 pJ/μm^2, effects of photo-induced losses on the modulated input result in a reduced contrast of the standing wave pattern and an overall reduction in $\Delta T/T$. There are some variations in $\Delta T/T$ values between modes and also between top and bottom outputs (Figure S5 in Supporting Information), which could indicate some imperfections in the device fabrication, as discussed further below. Results for the direct modulation scheme are summarized in Figure S6 of the Supporting Information and confirm the trends already discussed in Figure 3f.

As a first step toward understanding the interplay between standing wave photonic modes and plasmonic nanoantennas, we numerically calculate the response of a racetrack resonator with groups of three antennas on the top and bottom of the device using a three-dimensional FDTD model. Due to a rapidly increasing computation time with system size, we considered a model system with a reduced racetrack perimeter of 47 μm, which however gives a good qualitative agreement to our experiments. The racetrack is critically coupled to input and output waveguides, and a standing wave is launched by sending counter-propagating waves from the inputs. An initial phase difference $\Delta\varphi$ of -180° is applied to the top input arm, consistent with the experiment. In our calculations we are also able to examine the transmission of the through ports, corresponding to light reflected back into the MMI, which cannot be accessed in our experiment. Figures 5a and b present the output spectra and corresponding $\Delta T/T$ of the top and bottom drop port for several values of $\Delta\varphi$. Figures 5c and d shows the corresponding through port transmissions. The general behaviour at the drop ports agrees well with the experimental results of Figures 3e and f. In particular, the asymmetry in the response of the two output ports, corresponding to cross and direct pumping conditions, is reproduced faithfully by the simulation. Figures 5e and f directly compare the calculated and experimental transmission. The full experimental range corresponds approximately to a phase shift from -180° to -90°, as indicated by the grey shaded regions and consistent with earlier results.[25] In this range, we find similar trends between calculated and experimental peak intensities. At around a $\Delta\varphi$ of -90°, we observe a mode splitting of the odd mode, both in the calculated and experimental spectra and for the direct modulation configuration. Figures 5e and 4f furthermore reveal a symmetry between the even and odd modes when flipping the phase by 180°, which is expected intuitively as this operation simply transforms nodes to anti-nodes and vice versa. However, for intermediate phase shifts $\Delta\varphi$, the symmetry involves an additional flipping of the output ports. This additional permutation suggests that the phase plays a role in the behaviour at intermediate phase shifts, which is different from a purely intensity-dependent CPA effect.

Part of the changes in the through port transmission can be attributed to modification of the critical coupling condition due to antenna-waveguide interaction. Our devices are optimized for critical coupling of the unperturbed racetrack, therefore antenna-induced effects will modify the coupling efficiency. Simulated through-port transmission spectra [Figures 5c and d] show reduced coupling into the racetrack when the interaction with the antennas is strong. Critical coupling mismatch results in up to 30% of light transmitted via the through ports in our current design. Combining information from drop port and through port transmissions, we estimate coherent absorption by the antennas to reach around 50% of the incident intensity. Furthermore we note that critical coupling alone cannot explain observed mode splittings and asymmetry of the outputs.

The observed difference between the cross-modulation and direct-modulation schemes can be explained using a hybridization model commonly used to explain the scattering-induced mode splitting in photonic ring resonators.[28-30] While usually the model is applied to describe coupling to standing waves using a travelling wave input, here we consider the reverse situation, namely coupling to clockwise and counter-clockwise travelling waves from a standing-wave input. In the presence of a small scattering perturbation, the principal modes are the standing-wave modes defined as a superposition of the clockwise c and counter-clockwise (cc) modes $E_{+}=E_{c}+E_{cc}$ and $E_{-}=E_{c}-E_{cc}$, corresponding respectively to $\Delta\varphi = 0°$ and -180° in our work. At these phases the antennas are positioned exactly in the nodes or anti-nodes (considering the odd mode and odd number of antennas) and the response can be described by the individual modes E_+ and E_-, corresponding to maximum coupling and perfect transparency, respectively. Typically, hybridization between antenna and photonic modes introduces an energy splitting between E_+ and E_- [24, 29], which is responsible for the wavelength shift between λ_+ and λ_- seen in our experiment and numerical simulations. At intermediate phases, the response is given by a superposition of the principal modes according to $\mathrm{E}(\Delta\varphi)=E_+\cos\Delta\varphi/2+E_-\sin\Delta\varphi/2$. Thus, at $\Delta\varphi$=-90° the total intensity is given by $I=|(E_+-E_-)|^2/2=2|E_{cc}|^2$ while for $\Delta\varphi$=+90°, $I=|(E_++E_-)|^2/2=2|E_c|^2$. In other words, for phase shifts $\Delta\varphi$=±90° the output light from both input arms is converted into one of the clockwise and counter-clockwise modes. As the bottom and top output ports carry light from respectively the clockwise and counter-clockwise modes, the photon-plasmon hybridization thus results in an effective rerouting of light between output ports. The hybridization picture thus accounts for the asymmetry between outputs for intermediate phases where one output shows a reduced intensity while the opposite output shows an increased intensity.

Associated with the coherent photon-plasmon interaction is a local field enhancement around the nanoantennas. Figure 6a shows calculated near-field maps in the plane of the antennas (*xy*), directly above the top of the waveguide, for values of the phase shift $\Delta\varphi$ of -180° and 0°. The antenna field was normalized to the evanescent field, $E_{\mathrm{ev.}}$, of a reference waveguide at the same vertical position, as this directly provides the enhancement factor relevant for applications in field-enhanced spectroscopy. Figure 6a also shows the vertical (*xz*) cross section through the centre of the photonic waveguide, where we plot the field normalized to the maximum field, E_0, inside the reference waveguide ($E_0\approx1.85E_{\mathrm{ev.}}$) relevant to estimate the photonic field distribution. The transition from weak to strong photon-plasmon interaction with $\Delta\varphi$ is accompanied by an increase of the local near-field strength around the nanoantenna, and a reduction of the field in the photonic mode inside the racetrack. Values of the local field intensity at the antenna ends are shown in Figure 6b and indicate that the near-field intensity enhancement reaches values $>10^2$ with respect to the evanescent field of the reference waveguide. Further improvement of the field enhancement will be possible when using different antenna designs including dimers, nano-gaps, or sharp tips.

An important challenge is related to fabrication tolerances of both the silicon and plasmonic components needed to achieve reproducible device performance. As illustrated in the Figure S7 in Supporting Information, the transmission spectra are not always identical between top and bottom ports, which is most likely related to small nanofabrication errors in the SOI gratings and wavelength-dependent scattering losses in the racetrack, as can be seen in the darkfield images of Figure 2. Both the antenna darkfield intensity and normalized $\Delta T/T$ measurements appear less sensitive to these variations than the linear transmission through the device. Nanofabrication errors in the antenna placement provide a limit to the reproducibility. Figure S8 in Supporting Information shows that a positioning accuracy better than 25 nm is needed for antennas to perform within design tolerances, which is approaching the limits of multi-exposure lithography.

Further optimization of device geometries to exploit coherent photon-plasmon interactions will be of interest for a wide range of applications, as it may provide new nanoscale mechanisms for spectrally and spatially reconfigurable and switchable devices. The complex interplay between critical coupling, CPA, antenna-induced reflections and mode hybridization, and their dependence on antenna parameters will require more detailed modelling, as can be done for example using coupled-mode theory.[31] Further tuning of device performance toward CPA may require tailoring the antennas to suppress back-reflections, while simultaneously increasing the number of antennas to maintain high total interaction strength. For applications in optical routing, another set of requirements is needed by increasing reflections and reducing losses from the antennas, for example by increasing the antenna size. Critical coupling can be chosen to match the hybrid modes rather than the unperturbed resonances, for applications benefiting from maximum conversion to optical near-fields.[32] Efficient conversion of photonic guided modes to plasmonic hotspots with strong field localization outside the waveguide holds interest for a variety of applications in field-enhanced spectroscopy, sensing, and nonlinear optics. Future work should explore hybrid photonic and plasmonic circuits for all-optical control, using localized plasmonic absorption to drive ultrafast nonlinearity, with promise for all-optical signal processing devices.[33]

In conclusion, we experimentally demonstrate coherent absorption and mode hybridization in hybrid photonic-plasmonic resonators by fabricating gold nanoantenna arrays on SOI racetrack resonators. With two counter-propagating coherent waves circulating in the resonators, the resulting standing wave field interacts strongly with the nanoantennas located in the anti-nodes of respective resonances via plasmon excitation, leading to significant perturbation of specific racetrack resonances. Spectrally resolved light scattering by the nanoantennas confirms the selective coupling with the standing-wave pattern. Ultrafast optical control of the hybrid racetrack-nanoantenna system was achieved by inducing a nonlinear phase shift in one of the inputs, which shifted the standing waves in the racetracks and altered the photon-plasmon interaction strength. Experiments on different numbers of antennas reveal how the precise placement of broadband antennas dictates a narrowband spectral function through coherent interaction. Generalizing this concept and allowing for antennas to be placed strategically on any positions along the resonator gives a huge number of degrees of freedom to define which resonances, or groups of resonances, are to be absorbed. In such a way, a large number of degrees of freedom for circuit design can be explored to develop more and more complex on-chip functionalities within compact footprints.

ASSOCIATED CONTENT

Supporting Information. The Supporting Information is available free of charge via the Internet at http://pubs.acs.org. Experimental results showing light scattering from antennas, spatial modulation maps, photomodulation spectra, linear transmission spectra; numerical simulations showing effect of positioning error and near field enhancement maps.

AUTHOR INFORMATION

Corresponding Author

[*] E-mail: O.Muskens@soton.ac.uk

Present Addresses

[§] Roman Bruck: Luxtera, 320 Camino Vida Roble, Carlsbad, CA 92011, USA.

[§] Daniel Traviss: Coherent Inc., West of Scotland Science Park, G20 0XA, Glasgow, UK.

Author Contributions

The manuscript was written through contributions of all authors. All authors have given approval to the final version of the manuscript. The authors declare no competing financial interest.

ACKNOWLEDGMENT

The authors acknowledge C. Riedel and Z. Webber for their help in the fabrication of devices. The authors acknowledge support from EPSRC through grant EP/J016918/1 and EP/L00044X/1. OM acknowledges support by EPSRC through grant EP/M009122/1. The SOI samples were fabricated in the frame of the EPSRC CORNERSTONE project (EP/L021129/1). The dataset for this work can be found at 10.5258/SOTON/D0358.

REFERENCES

(1) Chong, Y.D.; Ge, L.; Cao, H.; Stone, A.D. *Phys. Rev. Lett.* **2010**, 105, 053901.

(2) Baranov, D. G.; Krasnok, A.; Shegai, T.; Alù, A.; Chong, Y. *Nat. Rev. Mater.* **2017**, 2, 17064 (2017).

(3) Wan, W.; Chong, Y.; Ge, L.; Noh, H.; Stone, A.D.; Cao, H. *Science* **2011**, 331, 889-892.

(4) Wong, Z. J.; Xu, Y.-L.; Kim, J.; O'Brien, K.; Wang, Y.; Feng, L.; Zhang, X. *Nat. Photonics* **2016**, 10, 796-801.

(5) Zhang, J.; MacDonald, K. F.; Zheludev, N. I. *Light: Sc. & Appl.* **2012**, 1, e18.

(6) Roger, T.; Vezzoli, S.; Bolduc, E.; Valente, J.; Heitz, J. J. F.; Jeffers, J.; Soci, C.; Leach, J.; Couteau, C.; Zheludev, N. I.; Faccio, D. *Nature Comm.* **2015**, 6, 7031.

(7) Feng, L.; Wong, Z. J.; Ma, R.-M.; Wang, Y.; Zhang, X. *Science* **2014**, 346, 972-975.

(8) Rothenberg, J. M.; Chen, C. P.; Ackert, J. J.; Dadap, J. I.; Knights, A. P.; Bergman, K.; Osgood, R. M.; Grote, R. R. *Opt. Lett.* **2016**, 41, 2537-2540.

(9) Bruck, R.; Muskens, O. L. *Opt. Expr.* **2013**, 21, 27662-27671.

(10) Schuck, P. J.; Fromm, D. P.; Sundaramurthy, A.; Kino, G. S.; Moerner, W. E. *Phys. Rev. Lett.* **2005**, 94, 017402.

(11) Giannini, V.; Fernández-Domínguez, A. I.; Heck, S. C.; Maier, S. A. *Chem. Rev.* **2011**, 111, 3888-3912.

(12) Zijlstra, P.; Paulo, P. M. R.; Orrit, M. *Nat. Nanotech.* **2012**, 7, 379-382.

(13) Novotny, L.; Van Hulst, N. *Nat. Photonics* **2011**, 5, 83-90.

(14) Punj, D.; Mivelle, M.; Babu Moparthi, S.; Van Zanten, T. S.; Rigneault, H.; Van Hulst, N. F.; García-Parajó, M. F.; Wenger, J. *Nat. Nanotech.* **2013**, 8, 512-516.

(15) Rodríguez-Fortuño, F. J.; Espinosa-Soria, A., Martínez, A. *J. Opt.* **2016**, 18, 123001.

(16) Arango, F. B.; Kwadrin, A.; Koenderink, A. F. *ACS Nano* **2016**, 6, 10156-10167.

(17) Vercruysse, D.; Neutens, P.; Lagae, L.; Verellen, N.; Van Dorpe, P. *ACS Photonics* **2017**, 4, 1398-1402.

(18) Guo, R.; Decker, M.; Setzpfandt, F.; Gai, X.; Choi, D.-Y.; Kiselev, R.; Chipouline, A.; Staude, I.; Pertsch, T.; Neshev, D. N.; Kivshar, Y. S. *Sci. Adv.* **2017**, 3, e1700007.

(19) Février, M.; Gogol, P.; Aassime, A.; Mégy, R.; Delacour, C.; Chelnokov, A.; Apuzzo, A.; Blaize, S.; Lourtioz, J.-M.; Dagens, B. *Nano Lett.* **2012**, 12 (2), 1032–1037.

(20) Février, M.; Gogol, P.; Barbillon G.; Aassime, A.; Mégy, R.; Bartenlian, B.; Lourtioz, J.-M.; Dagens, B. *Opt. Express* **2012**, 20, 17402-17410.

(21) Peyskens, F.; Dhakal, A.; Van Dorpe, P.; Le Thomas, N.; Baets, R. *ACS Photonics* **2016**, 3, 102-108.

(22) Luo, Y.; Chamanzar, M.; Apuzzo, A.; Salas-Montiel, R.; Ngoc Nguyen, K.; Blaize, S.; Adibi, A. *Nano Lett.* **2015**, 15 (2), 849-856.

(23) Doeleman, H. M.; Verhagen, E.; Koenderink, A. F. *ACS Photonics* **2016**, 3, 1943-1951.

(24) Ameling, R.; Giessen, H. *Nano Lett.* **2010**, 10 (11), 4394–4398.

(25) Bruck, R.; Mills, B.; Troia, B.; Thomson, D. J.; Gardes, F. Y.; Hu, Y.; Mashanovich, G. Z.; Passaro, V. M. N.; Reed, G. T.; Muskens, O. L. *Nat. Photon.* **2015**, 9, 54–60.

(26) Turner-Foster, A. C.; Foster, M. A.; Levy, J. S.; Poitras, C. B.; Salem, R.; Gaeta, A. L.; Lipson, M. *Opt. Express* **2010**, 18, 3582-3591.

(27) Kampfrath, T.; Beggs, D. M.; White, T. P.; Burresi, M.; Van Oosten, D.; Krauss, T. F.; Kuipers, L. *Appl. Phys. Lett.* **2009**, 94, 241119.

(28) Little, B. E.; Chu, S. T.; Haus, H. A. *Opt. Lett.* **1998**, 23, 1570-1572.

(29) Mazzei, A.; Götzinger, S.; Menezes, L. S.; Zumofen, G.; Benson, O.; Sandoghdar, V. *Phys. Rev. Lett.* **2007**, 99, 173603.

(30) Zhu, J.; Ozdemir, S. K.; Xiao, Y.-F.; Li, L.; He, L.; Chen, D.-R.; Yang, L. *Nat. Photonics* **2010**, 4, 46 - 49.

(31) Fauché, P.; Kosionis, S. G.; Lalanne P. *Phys. Rev. B* **2017**, 95, 195418

(32) Chamanzar, M.; Adibi, A. *Opt. Expr.* **2011**, 19, 22292.

(33) Khurgin, J.B.; Sun, G.; Chen, W.T.; Tsai, W.-Y.; Tsai, D. P. *Sc. Rep.* **2015**, 5, 17899.

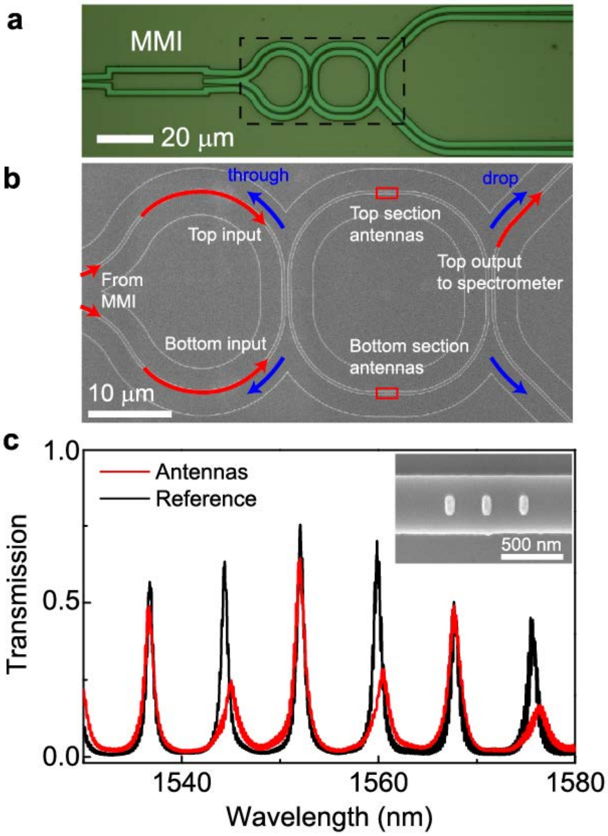

Figure 1 SEM images and transmission of nanoantenna-integrated racetrack resonators. (a) Optical microscopy image of device with MMI coupler and (b) SEM image of detail of a showing the racetrack resonator. Nanoantenna arrays are located on the top and bottom straight sections of the racetrack. (c) Transmission spectrum of the top output for device with groups of three antennas (SEM in inset) (red) and reference device without antennas (black).

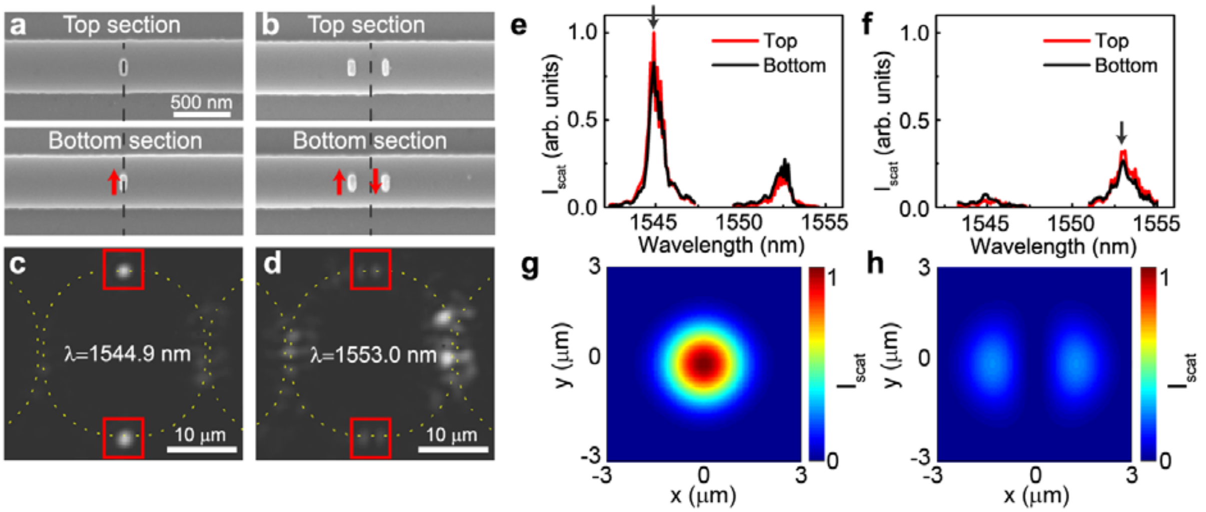

Figure 2 Investigation of light scattered from antennas. (a,b) Detailed SEM images of devices with one and two antennas per group. Arrows indicate phase of the standing wave E-field. (c,d) Scattering collected from devices with one and two antennas respectively, for wavelengths of maximum intensity. (e,f) Nanoantenna scattering spectra collected from top and bottom antenna groups for devices in (c,d). (g, h) Calculated point spread functions for devices with one (a,c) and two (b,d) nanoantennas driven by a standing wave *E*-field.

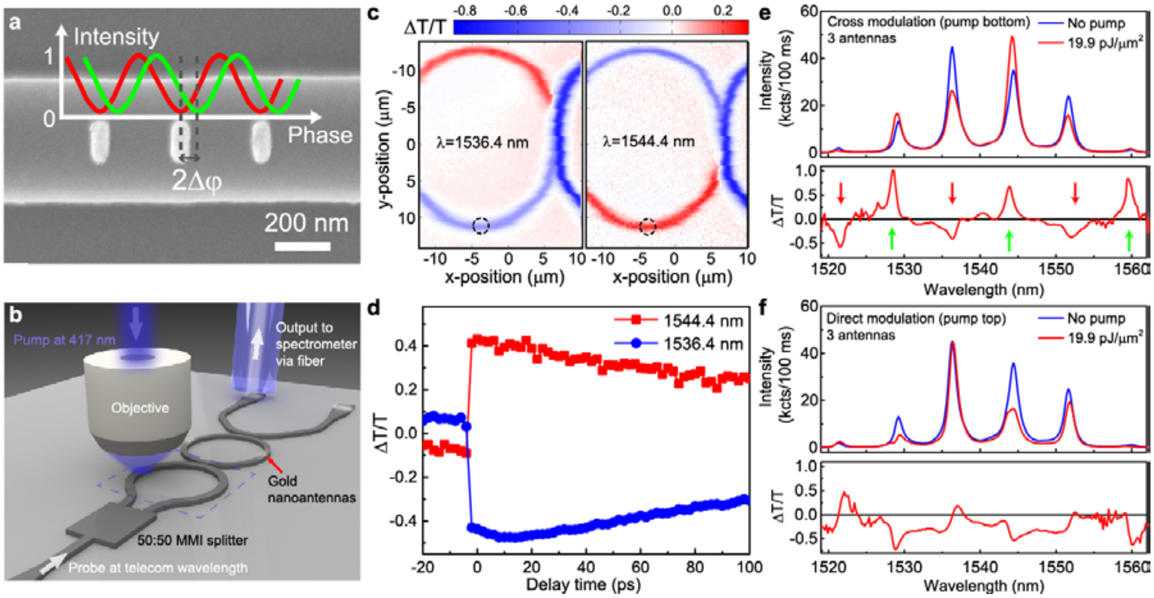

Figure 3 Tuning the coherent absorption by introducing an ultrafast photomodulation. (a) Illustration of standing wave intensity profile without perturbation (red) and including a phase perturbation $\Delta\varphi$ in one of the arms (green), resulting in shift of intensity pattern by $2\Delta\varphi$. (b) Schematic of the UPMS setup, dashed line: scan area. (c) Spatial maps over the input coupler region (scan area in b) at 5 ps delay time and (d) time dependence of photomodulation amplitude ΔT/T for wavelengths of 1536.4 nm and 1544.4 nm. (e, f) Top output spectra from the 3-nanoantenna racetrack resonator in Figure 1a for pump on the bottom (e) and top (f) input waveguides.

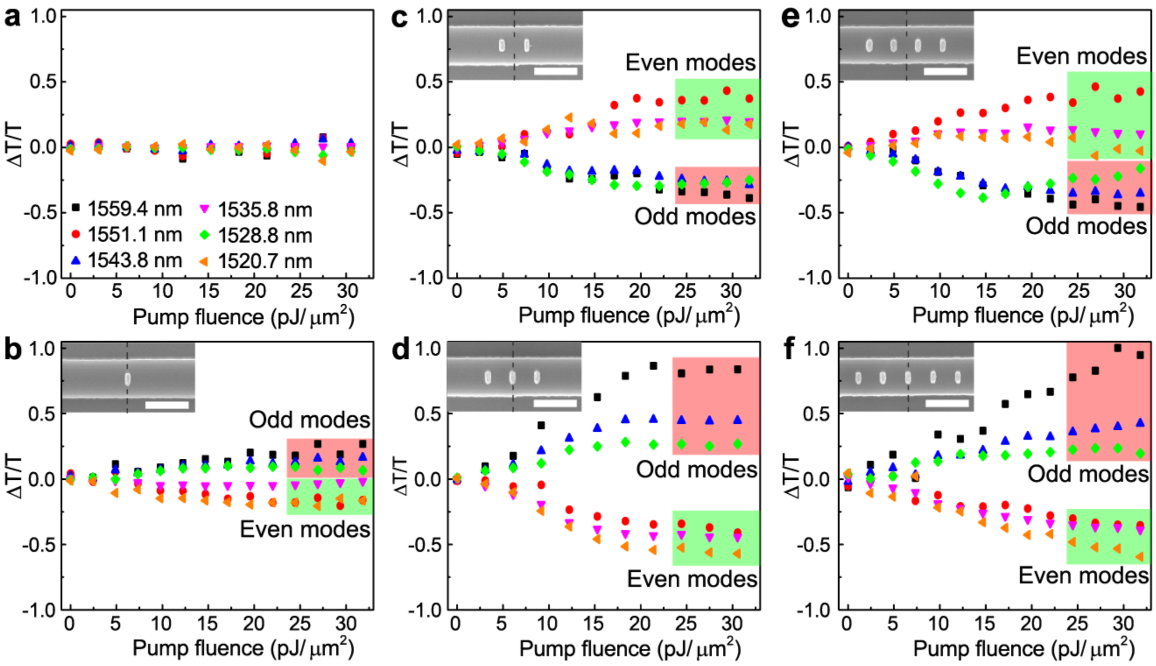

Figure 4 Modulation depth Δ*T*/*T* of racetracks with different numbers of nanoantennas. (a-f) Cross-modulation depths Δ*T*/*T* of top outputs from five racetracks which have the nanoantenna arrays with element numbers from 0 to 5. Six resonant modes are included, in which odd modes and even modes are grouped in green and red shapes, respectively. The insets show the SEM images of the nanoantennas on the racetrack around position -*L*/4 (dashed line). Scale bar, 500 nm.

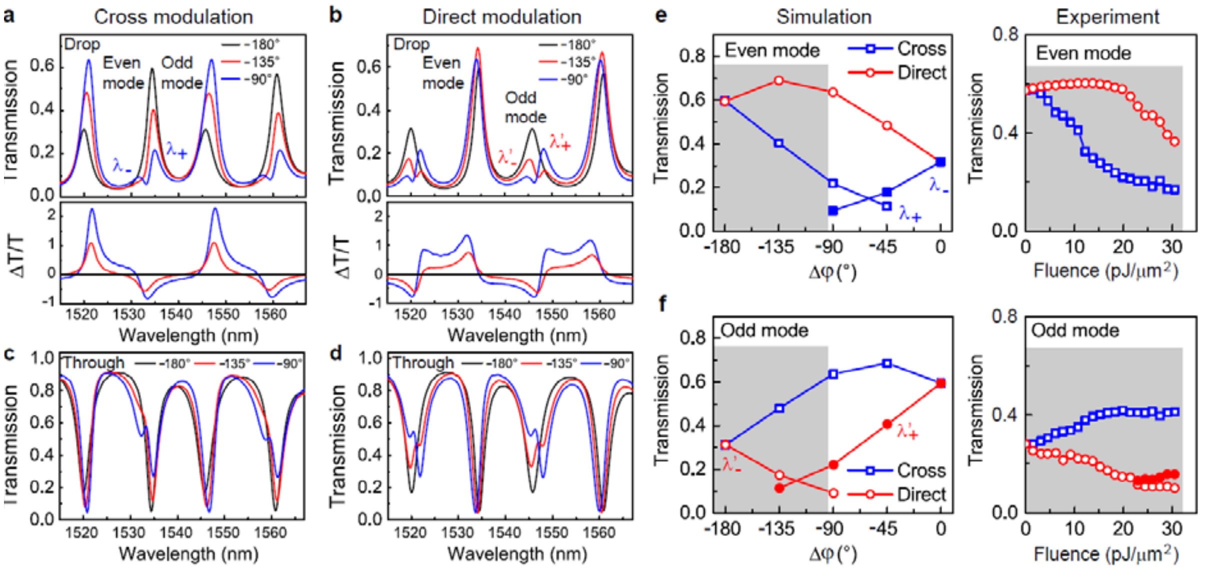

Figure 5 Simulation of the racetrack resonator with nanoantennas. (a, b) Top drop port transmissions and corresponding ΔT/T for cross-modulation (a) and direct modulation (b) and for values of Δ*φ* of -180°, -135°, and -90°. (c, d) Through port transmission corresponding to (a) and (b). (e, f) Extracted simulated and experimental values of the drop port transmission against Δ*φ* for even modes (e) and odd modes (f). Shaded areas of simulation and experiment map onto each other, a pump fluence of 30 pJ/μm^2 corresponding approximately to Δ*φ*=-90°.

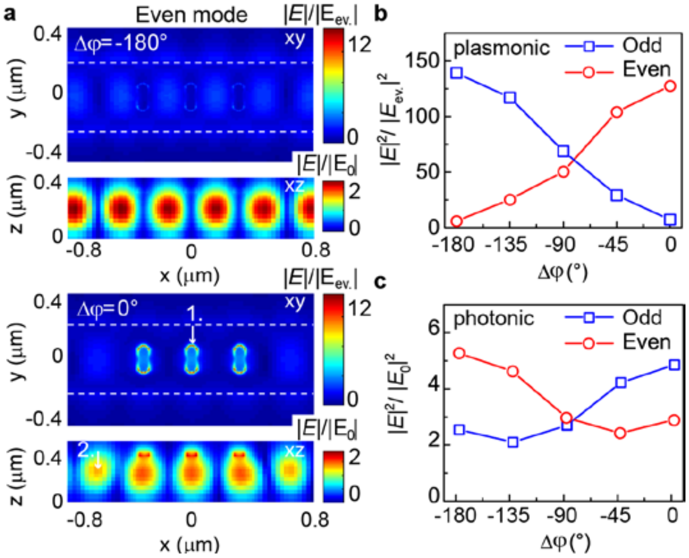

Figure 6 Simulation of near fields. (a) Electric field magnitude at the antenna plane for the even mode around λ=1534.4nm, for Δ*φ*=180° and 0°. (b) Near-field intensity $|E|^2$ near the tip of the centre plasmonic antenna for the even and odd modes. (c) Same for photonic mode amplitude in the *xz* images. Fields in (b, c) were normalized to evanescent field ($E_{ev.}$) and core (E_0) of reference waveguide, respectively.

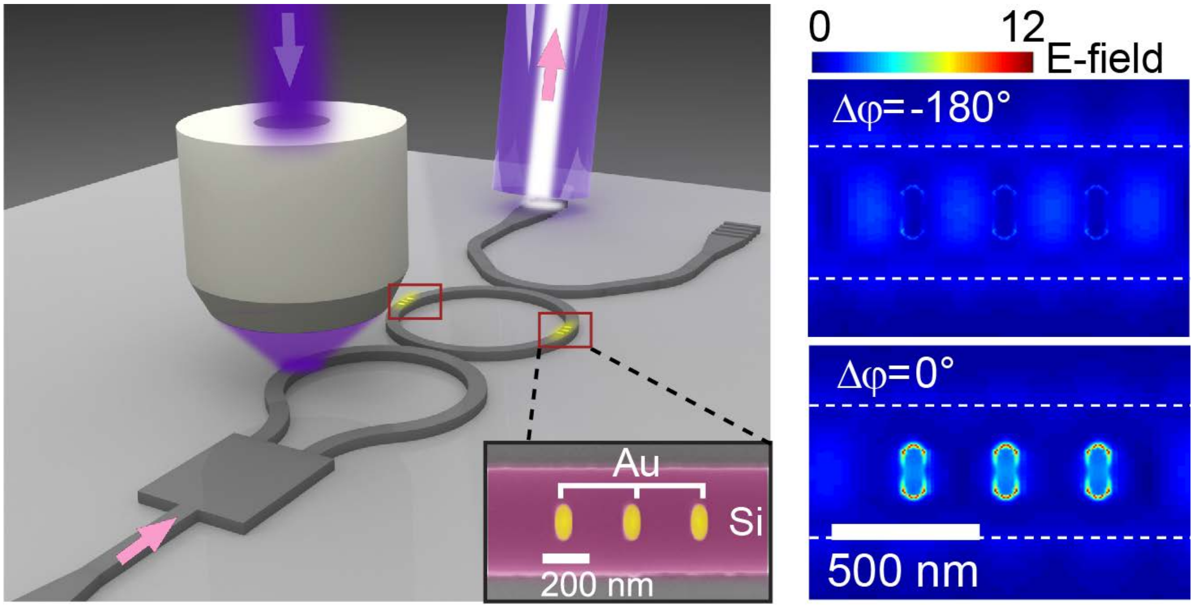

Table of Contents Figure